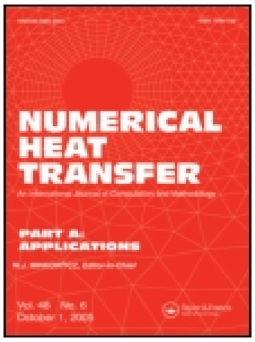

Numerical Heat Transfer, Part A: Applications

An International Journal of Computation and Methodology

ISSN: 1040-7782 (Print) 1521-0634 (Online) Journal homepage: http://www.tandfonline.com/loi/unht20

LES of convective heat transfer and incompressible fluid flow past a square cylinder

Xiaowang Sun, C. K. Chan, Bowen Mei & Zuojin Zhu

NUMERICAL HEAT TRANSFER, PART A
2016, VOL. 69, NO. 10, 1106–1124
http://dx.doi.org/10.1080/10407782.2015.1109386

Taylor & Francis
Taylor & Francis Group

LES of convective heat transfer and incompressible fluid flow past a square cylinder

Xiaowang Sun[a], C. K. Chan[b], Bowen Mei[a], and Zuojin Zhu[a,b]

[a]Faculty of Engineering Science, University of Science and Technology of China, Hefei, P.R. China; [b]Department of Applied Mathematics, The Hong Kong Polytechnic University, Kowloon, Hong Kong

ABSTRACT
This paper presents large eddy simulation (LES) results of convective heat transfer and incompressible-fluid flow around a square cylinder (SC) at Reynolds numbers in the range from 10^3 to 3.5×10^5. The LES uses the swirling-strength based sub-grid scale (SbSGS) model. Several flow properties at turbulent regime are explored, including lift and drag coefficients, time-spanwise averaged sub-grid viscosity, and Kolmogorov micro-scale. Local and mean Nusselt numbers of convective heat transfer from the SC under isothermal wall temperature are predicted and compared with empirical results.

ARTICLE HISTORY
Received 23 June 2015
Accepted 28 August 2015

1. Introduction

Incompressible turbulent flows past a square cylinder (SC) are important in engineering science, and numerical solutions are useful for the understanding of the flow characteristics. A literature review for the work before 1990 was given previously by Zhu [1], and some academic backgrounds are addressed in this paper.

The heat transfer from SC was measured by Hilpert [2] and Igarishi [3], as reported in [4, 5]. The experimental work of Igarashi was done in a low speed wind tunnel with rectangular cylinders of height 30 mm heated under constant heat flux. After the wake flow measurements [6–11], Lyn and Rodi [12] conducted some experiments on the flapping shear layer formed by flow separation from the forward corner of a SC, with the associated recirculation region on the sidewall, and they found that the recirculation is an important aspect of some flow properties. For drag forces acting on flat-sided columns, the study encompassed by Tong et al. [13] revealed all chamfering can reduce the drag compared with the sharp-cornered case.

Together with the experimental studies reported recently [14–18], there are also numerical simulations [19–34], some based on the k–ε turbulence model [19–21] or direct numerical simulation (DNS) [22–32], with others by means of large eddy simulation (LES) [33, 34]. For turbulent flow simulations, three strategies, phenomenological modeling [35, 36], DNS [37], and LES [38], are usually employed. In recent years, as reported widely [38–46], LES has become a viable and popular simulation tool.

For LES, in addition to the earlier sub-grid scale (SGS) model of Smagorinsky [38], many SGS models have been developed, including the dynamic SGS model given by Germano et al. [47], a subsequent modification given by Lilly [48], the SGS model based on the Kolmogorov equation for resolved turbulence given by Cui et al. [49, 50], the model based on algebraic theory [51], the model assuming sub-grid stress to be proportional to the temporal increment of filtered strain rate by

CONTACT Zuojin Zhu Zuojin@ustc.edu.cn Faculty of Engineering Science, University of Science and Technology of China, Jin Zhai Road 96, Hefei 230026, P.R. China.
Color versions of one or more of the figures in the article can be found online at www.tandfonline.com/unht.

Nomenclature

$\mathbf{A}$	matrix expression of velocity gradient $\nabla \mathbf{u}$	$\mathbf{u}$	velocity vector
a_{ij}	element of matrix $\mathbf{A}$	u_{in}	incoming flow speed (m/s)
B	spanwise length of square cylinder (m)	u, v, w	normalized velocity components (m/s)
C_μ	artificially defined constant in Eq. (1)	x, y, z	Cartesian coordinates
d	cross-sectional side length of SC (m)	ε	dissipation rate of k
f_I	FSI, factor of swirling-strength intermittency, given by Eq. (2)	λ_{ci}	swirling-strength (1/s)
		$\lambda = \lambda_{cr} + i\lambda_{ci}$	eigenvalue of $\nabla \mathbf{u}$
$k = \frac{1}{2}\overline{u_i'^2}$	turbulence kinetic energy	ρ	fluid density (kg/m^3)
Nu_m	mean Nusselt number	ν	fluid kinematic viscosity (m^2/s)
p	normalized pressure	ν_s	sub-grid viscosity (m^2/s)
$\mathrm{Re} = du_{\mathrm{in}}/\nu$	Reynolds number	$\nu_{sr} = \nu_s/\nu$	viscosity ratio
$S^{\max}$	assumed allowable total error	$(\nu_{sr})_{pm}$	time-averaged $(\nu_{sr})_{\mathrm{peak}}$
T	temperature (K)	$(\nu_{sr})_p'$	root mean square of $(\nu_{sr})_{\mathrm{peak}}$
T_w	temperature on SC wall surface (K)	$(\nu_{sr})_{\mathrm{peak}}$	peak value of ν_{sr}
T_∞	temperature of incoming flow fluid	Θ	normalized temperature
		θ	normalized temperature fluctuation

Zhu et al. [52], the singular valued SGS model [53], and the recent SGS model based on dynamic estimation of Lagrangian time scale given by Verma and Mahesh [54].

In LES the unclosed stresses are usually modeled by SGS-viscosity models. Alternatively, the nonlinear convective terms may be modified directly \citepHolm, based on these regulations [56–59]. The concept of spectral-vanishing-viscosity can be used to mimic SGS model for LES [60–64].

Turbulent flow is intermittent such that at a local point the flow may be swirling or non-swirling. The commonly used SGS models [38] have assigned artificially dependent sub-grid viscosity without taking care of the intermittency. A novel SGS model has been developed more recently [65, 66], which properly models turbulent flow intermittency.

This paper presents LES results for zero-incident incompressible turbulent flows around a single SC with convective heat transfer under constant wall temperature condition at Reynolds numbers in

Table 1. Computational parameters.

x_u/d	x_d/d	y_b/d	y_t/d	N_1	N_2	N_3	R_S^a
8.5	15	8.5	8.5	191	145	41	0.819

[a] $S^{\max} \approx 0.5\%$, with actual number if time steps n=13800 relevant to the final time t=170.

Table 2. Re dependence of CL, CD, $(\nu_{sr})pm$, the relevant RMS values, and the Strouhal number.

Re_3^a	CL	CD	$(\nu_{sr})pm$	CL$'$	CD$'$	$(\nu_{sr})_p'$	St
1	−0.0027	1.543	0.5567	0.1440	0.0346	0.1021	0.1079
2	−0.00542	1.560	1.726	0.120	0.0643	0.3311	0.1079
2.5	−0.00913	1.594	2.338	0.1302	0.0734	0.5841	0.1079
5.	−0.0250	1.736	5.197	0.1711	0.0781	1.194	0.1079
7.5	−0.0330	1.770	8.133	0.1776	0.0854	1.705	0.1079
10	−0.0365	1.788	10.971	0.1817	0.0877	2.723	0.1079
12.5	−0.0345	1.786	13.959	0.1726	0.0892	3.365	0.1079
25	−0.0359	1.813	28.953	0.1748	0.0979	6.562	0.1079
50	−0.0359	1.804	58.421	0.1612	0.0986	14.15	0.1079
75	−0.0369	1.834	82.453	0.1779	0.1048	16.66	0.1079
100	−0.0374	1.816	109.57	0.1624	0.1019	24.85	0.1079
125	−0.0370	1.825	146.23	0.1679	0.1013	34.14	0.1079
150	−0.0365	1.834	172.91	0.1721	0.1016	39.98	0.1079
200	−0.0373	1.832	228.38	0.1708	0.1024	43.92	0.1079
250	−0.0370	1.833	290.74	0.1710	0.1022	71.81	0.1079
275	−0.0369	1.845	292.59	0.1789	0.1040	60.42	0.1079
300	−0.0369	1.841	342.65	0.1817	0.1081	65.17	0.1079
325	−0.0367	1.843	366.75	0.1795	0.1046	81.55	0.1079
350	−0.0374	1.834	404.23	0.1725	0.1042	89.92	0.1079

[a] Note that $\mathrm{Re}_3 = \mathrm{Re}/10^3$.

the range of $\mathrm{Re} \in [10^3, 3.5 \times 10^5]$. Nineteen scenarios are presented, as shown in in Table 2, where the SbSGS model is described [65, 66], with the turbulent heat flux expressed under the gradient diffusion assumption [52, 67]. The objective of this paper is to explore numerically the characteristics of the heat and fluid flows past a SC, with particular reference to the three aspects of Reynolds number dependence, distributions of *t–z* averaged sub-grid viscosity ratio and Kolmogorov micro-scale, and the local and mean Nusselt numbers.

2. Governing equations

2.1. SbSGS model

At higher Reynolds numbers, effects of turbulence are very intense and crucial [37]. The effect of SGS on large scale motions must be considered carefully. As discussed in the literature [39–46], the sub-grid stress is postulated usually to be proportional to the local filtered strain rate, with a factor called sub-grid viscosity. This is analogous to Newtonian constitutive relationship for laminar flows, implying that these SGS models have not ascertained satisfactorily the validity of the range of Reynolds numbers.

In the earlier model of Smagorinsky [38], the sub-grid viscosity is proposed to be proportional to the modular of local filtered strain rate. Unfortunately, using three-dimensional velocity fields based on flow instability analysis [68], numerical tests revealed that peak values of the modular of strain rate occur at regions without swirling. To avoid this ambiguity, and considering turbulent flows having vortical structures and intermittency, a relatively fresh SbSGS model [65, 66] is employed.

Assuming that the sub-grid viscosity is proportional to the factor of swirling-strength intermittency (FSI) and local swirling-strength,

$$\nu_s = C_\mu f_I(\mathbf{x}, t)\lambda_{ci}\delta^2 \tag{1}$$

Here $C_\mu(=0.09)$ is an artificially defined constant; λ_{ci} is the swirling-strength of filtered velocity gradient $\nabla\mathbf{u}$, the FSI denoted by f_I, is defined by the ratio of swirling-strength λ_{ci} to the magnitude of the complex eigenvalue $\lambda(=\lambda_{cr} + i\lambda_{ci})$ of $\nabla\mathbf{u}$, i.e.,

$$f_I(\mathbf{x}, t) = \frac{\lambda_{ci}}{\sqrt{\lambda_{cr}^2 + \lambda_{ci}^2}} \tag{2}$$

where δ is the length scale, defined by harmonic-average of grid intervals

$$\frac{1}{\delta} = \sum_{i=1}^{3} 1/\delta_i \tag{3}$$

where δ_i denotes the grid interval in x_i direction. If the filtered velocity gradient $\nabla\mathbf{u}$ is denoted by

$$\nabla\mathbf{u} = \mathbf{A} = \begin{pmatrix} a_{11} & a_{12} & a_{13} \\ a_{21} & a_{22} & a_{23} \\ a_{31} & a_{32} & a_{33} \end{pmatrix} \tag{4}$$

its eigenvalue λ satisfies the characteristic equation

$$\lambda^3 + b\lambda^2 + c\lambda + d = 0 \tag{5}$$

where

$$\begin{cases} b = -\mathrm{tr}(\mathbf{A}) = -(a_{11} + a_{22} + a_{33}), \\ c = \begin{vmatrix} a_{22} & a_{23} \\ a_{32} & a_{33} \end{vmatrix} + \begin{vmatrix} a_{11} & a_{12} \\ a_{21} & a_{22} \end{vmatrix} + \begin{vmatrix} a_{11} & a_{13} \\ a_{31} & a_{33} \end{vmatrix}, \quad d = -|\mathbf{A}| \end{cases} \tag{6}$$

with $|\mathbf{A}|$ being the determinant of matrix $\mathbf{A}$. For incompressible flows, $b = 0$. For non-rotating coordinates, the roots of Eq. (5) are real when the local flow is temporally laminar. When the local flow becomes turbulent spontaneously, the roots have two conjugate complex eigenvalues denoted by $\lambda_{cr} \pm i\lambda_{ci}$, where $i(=\sqrt{-1})$ is the unit of imaginary number. Iso-surfaces of swirling-strength have been used to illustrate vortices in turbulent flows previously [69–71].

Assigning the parameter C_μ to be the same value as that used to define turbulent eddy viscosity of phenomenological models [35], the relevant value in the sub-grid model of Vreman [51] has been set as $2.5C_S^2$. While $C_S = 0.17$ is the theoretical value for homogeneous isotropic turbulence [72], suggesting a parametric value of 0.07. Furthermore, to accomplish robust simulations in complex cases the practical value of C_S is usually higher. For example, $C_S = 0.2$ has frequently been used in literature, giving a value 0.1. It is noted that in the SGS model of Germano et al. [47], the relevant coefficient is obtained by grid and test-grid filtering, and the coefficient is temporally and spatially changing, hence such kind of model is called a dynamic model.

As the sub-grid viscosity ν_s has a factor f_I, the decaying factor of length scale $[1 - \exp(-y^+/25)]$ near the wall as used by Moin and Kim [39] is not used in the present study.

It is noted that swirling-strength does not vanish completely in laminar flows under a rotating framework. To observe the difference in different SGS models, a comparison of the present SbSGS model with that of Vreman [51] is given in Figures 1*a*, *b*, where two top-views of the contours of sub-grid viscosity are illustrated. It can be seen that the sub-grid viscosity based on the present model is zero if the local flow is non-swirling, while sub-grid viscosity based on the Vreman's SGS model does not hold.

2.2. Governing equations

Consider the turbulent SC flow in a Cartesian coordinate system, as schematically shown in Figure 2, in which $x(x_1)$ is the horizontal coordinate, with $y(x_2)$ and $z(x_3)$ denoting the vertical and spanwise directions. The origin is allocated at the left-bottom corner of the SC. Let the incoming flow velocity be u_{in}, the Reynolds number of the SC flow can be defined by Re $= u_{\text{in}}d/\nu$.

Taking the length scale as the SC cross-sectional side length d, the time and pressure scales are $t_0 = d/u_{in}$ and ρu_{in}^2, where ρ is the fluid density. Therefore, for the zero-incident incompressible heat and fluid flow past a SC, the dimensionless governing equations have the following form:

$$\nabla \cdot \mathbf{u} = 0 \tag{7}$$

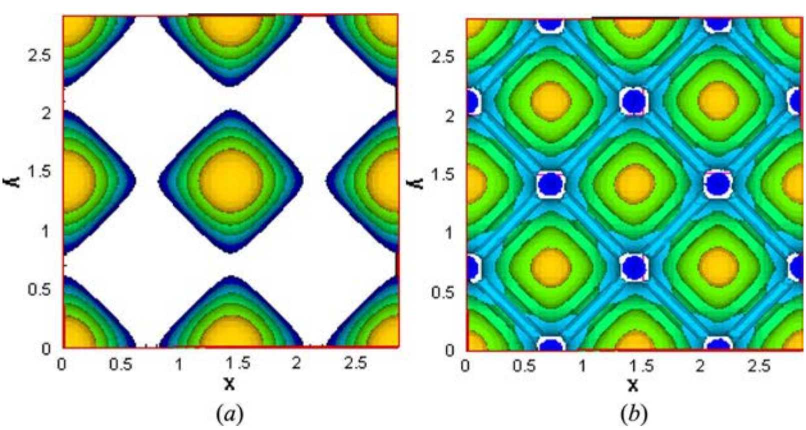

Figure 1. The comparison of the sub-grid model with the previous one proposed by Vreman [51]. (*a*) A top-view of the contours of ν_s based on the present model; (*b*) a top-view of the contours of ν_s based on the Vreman's model. Note that the sub-grid viscosity has a unit of W_0d_0 as seen in Appendix A. The contours in part (*a*) are labeled by values from 0.0004 to 0.0016 with an increment of 0.0003, while the contours in part (*b*) are labeled by values from 0.0004 to 0.012 with an increment of 0.0029.

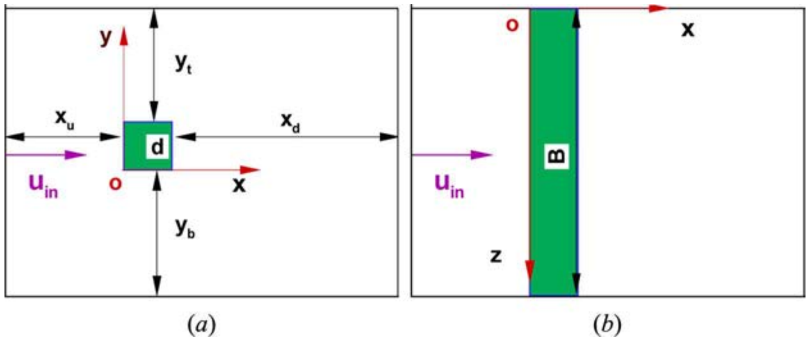

Figure 2. Schematic of the flow past a single SC. (*a*) *x*–*y* plane and (*b*) *x*–*z* plane.

$$\mathbf{u}_t + \mathbf{u} \cdot \nabla \mathbf{u} = -\nabla p + \nabla \cdot [\gamma_1 \nabla \mathbf{u}] + \mathbf{R} \tag{8}$$

$$\Theta_t + \mathbf{u} \cdot \nabla \Theta = \nabla \cdot [\gamma_2 \nabla \Theta] \tag{9}$$

where $\Theta = \frac{T - T_\infty}{T_w - T_\infty}$, T_w is the temperature on SC wall surface, with T_∞ being the temperature of incoming flow fluid. For simplicity, we have omitted the over bar for filtering of variables. The normalized total viscosities γ_1 and γ_2 can be represented by

$$\gamma_1 = \frac{1}{\mathrm{Re}}\left(1 + \frac{\nu_s}{\nu}\right), \quad \gamma_2 = \frac{1}{\mathrm{Re\,Pr}}\left(1 + \frac{\nu_s}{\sigma_\theta \nu}\right) \tag{10}$$

where the turbulent Prandtl number σ_θ is assumed to be 0.9, while **R** is a force related to the gradient of viscosity γ_1, given by

$$\mathbf{R} = (\nabla \mathbf{u})^T \cdot \nabla \gamma_1 \tag{11}$$

Uddin et al. [67] assigned some heat flux models in the LES of heat transfer caused by the normal impingement of air jet. Smirnov and Nikitin [36] provided a turbulent model for hydrogen combustion in engines. Here, we use the gradient diffusion assumption as previously [52], and assuming constant Prandtl number σ_θ, we have

$$-\overline{u_j'\theta} = \frac{\nu_s}{\sigma_\theta} \frac{\partial \Theta}{\partial x_j} \tag{12}$$

where u_j' denotes velocity fluctuation in the x_j direction, with θ being the temperature fluctuation.

The solutions of Eqs. (7)–(9) are sought under appropriate conditions. For the boundary conditions (BC) on the SC walls, constant wall temperature and non-slip BC are used, implying that

$$u = 0, \quad v = 0, \quad w = 0, \quad \Theta = 1 \tag{13}$$

while for the BC at the outlet, similar to the treatment [24, 25], we use the Orlanski type [73]

$$\varphi + u_c \varphi = 0, \tag{14}$$

where in normalized form, $u_c = 1$, $\varphi = (u, v, w, \Theta)^T$, with the superscript T representing the transpose of matrix (u, v, w, Θ). At the inlet section, no artificial velocity and temperature disturbances are assumed, such that

$$u = 1, \quad v = 0, \quad w = 0, \quad \Theta = 0 \tag{15}$$

On the lower and upper side boundaries of the computational domain, we use

$$u_y = 0, \quad v = 0, \quad w = 0, \quad \Theta_y = 0 \tag{16}$$

On the spanwise boundaries, periodic condition is used such that

$$\varphi(x, y, z, t) = \varphi(x, y, z + B, t) \tag{17}$$

where B is the spanwise (z) length of SC as shown in Figure 2. The initial condition is given by

$$u = 1, \quad v = 0, \quad w = 0, \quad \Theta = 0 \tag{18}$$

3. Numerical method

3.1. Solution procedure

The governing Eqs. (7)–(9) of the heat and fluid flows past a single SC are discretized by a finite difference method in a staggered grid system, where the convective terms are treated using a fourth-order upwind scheme [74]. By making some changes, the existing numerical methods, such as described [75–86] are also applicable. The simple approach recently reported by Trias et al. [87], which on any structured or unstructured grid can be implemented easily, is also suitable for LES of incompressible flows.

The solutions procedure is based on the accurate projection algorithm PmIII developed by Brown et al. [88]. Let intermediate velocity vector, pressure potential, and time level be $\bar{\mathbf{u}}$, ϕ, and n, respectively. Denoting $\mathbf{H} = (\mathbf{u}\cdot\nabla)\mathbf{u} - \mathrm{R}$, then letting

$$\mathbf{u}^{n+1} = \bar{\mathbf{u}} - \Delta t \nabla \phi \tag{19}$$

we can calculate $\bar{\mathbf{u}}$ by means of

$$\frac{\bar{\mathbf{u}} - \mathbf{u}^n}{\Delta t} + \mathbf{H}^{n+1/2} = \nabla \cdot \left\{ \gamma_1 \nabla \left[\mathbf{u}^n + \frac{1}{2}(\bar{\mathbf{u}} - \mathbf{u}^n) \right] \right\} \tag{20}$$

and calculate pressure p by

$$p^{n+1/2} = \{1 - 0.5(\Delta t)\nabla \cdot [\gamma_1 \nabla]\}\phi \tag{21}$$

where the pressure potential ϕ satisfies the Poisson's equation

$$\nabla^2 \phi = \nabla \cdot \bar{\mathbf{u}} / \Delta t \tag{22}$$

The temperature Θ^{n+1} can be calculated by

$$\frac{\Theta^{n+1} - \Theta^n}{\Delta t} + H_4^{n+1/2} = \nabla \cdot \left\{ \gamma_2 \nabla \left[\Theta^n + \frac{1}{2}(\Theta^{n+1} - \Theta^n) \right] \right\} \tag{23}$$

where $H_4 = (\mathbf{u}\cdot\nabla)\Theta$, and the terms at the level of $(n + 1/2)$ are calculated explicitly using the second-order Adams–Bashforth formula [89]. Nonlinear convective terms in the governing equations are spatially discretized by a fourth-order upwind finite difference scheme [74], with viscous diffusion terms by a second-order central difference scheme.

The pressure potential Poisson's equation is initially solved by the approximate factorization one (AF1) method [90], and subsequently corrected by the stabilized bi-conjugate gradient method (Bi-CGSTAB) given by Van der Vorst [91] to improve its accuracy. In the AF1 application, for SC wake flow simulation, the numerical experience reported elsewhere [1] is useful for numerical stability of pressure potential iteration. The criterion for pressure potential iteration is chosen so that the relative error defined [89] is less than 1×10^{-7}. In spatial discretization, the implicit second-order Crank–Nicolson method is used to solve the diffusion terms on right-hand side in a non-standard way, where the part depending on the viscosity gradient ($\nabla\gamma_1$) in Eq. (10) is calculated explicitly, while the remaining part denoted by $[\nabla\cdot(\gamma_1\nabla\mathbf{u})]$ is calculated implicitly.

3.2. Reliability evaluation

In the recent numerical study of Smirnov et al. [92], simulating hydrogen fuel rocket engines using LOGOS simulator [93], an approach for predicting accumulated error in numerical work based on Navier–Stokes equations was reported in detail. As the diffusive terms are treated with the second-order central difference scheme, using the values of N_1, N_2, and N_3 as given in Table 1, and the assumed allowable total error $S^{\max} = 0.5\%$, the ratios of maximum allowable number of time steps to the actual number of time steps used to obtain the result, $R_s = 0.819$, are estimated and shown in Table 1. This ratio estimation has indicated reliability of the LES results, as reported by Smirnov et al. [92]. The ratio R_s characterizes reliability of results, i.e., how far below the limit the simulations were finalized. Indirectly it characterizes the accumulated error. The higher the value R_s is, the lower is the error. As R_s approaches to unity the error tends to the maximum allowable value.

4. Results and discussion

Using the solution method given above, LES of heat and fluid flows past a single SC, as shown schematically in Figure 2, was encompassed in a personal computer with a memory of 3.2 Gb and CPU frequency 3.30 GHz. Each case requires a CPU time of about 86 hours. As can be seen in Table 2, classified by $\mathrm{Re}_3 = \mathrm{Re}/10^3$, 19 scenarios were studied in the LES work. For each scenario the spanwise length of the SC (B) is set at 4.

In the z-direction, the grid is uniform with number N_k set as 41. While the grids are non-uniform in the x- and y-directions, the grid-numbers are set at 191 and 145, respectively, with grid arrangements based on a geometric-series algorithm [65]. In this LES, the assignment of grids on the SC section walls uses two key parameters of amplifying-factor (1/0.847) and series termination number (14). The total number of vertical grid-line through the SC cross-sectional side is 34.

At the bottom and top of the SC, the y-grid is assigned with an amplifying-factor of 1/0.9 and a series-termination number of 37. For the x-grid, the relevant values are 1/0.817 and 17, respectively, for the region upstream of the SC, but 1/0.927 and 47 for the region downstream of the SC. Using a geometric-series algorithm for grid partition, it can be seen that the finest grid distance to each SC wall is $2.733 \times 10^{-3}d$. Such a grid arrangement leads to a time step of $\Delta t = 1.25 \times 10^{-3}$, which is smaller than that used in the LES reported [65].

To show the distribution of Kolmogorov micro-scale in the x–y plane, time-spanwise (t–z) averaging is used. A subscript m is used to represent the t–z averaged variables, with a symbol $'$ used to denote the root mean square (RMS) values of the variables. The subscript m is omitted for t–z average lift (CL) and drag (CD) for simplicity. Furthermore, grid spacing and time step for the 19 scenarios remain the same. To remove the effect of initial condition, data in the time period of $t \in [68, 170]$ are processed.

4.1. Fluid flow characteristics

For turbulent SC flows, the flow induced forces acting on SC, usually decompose into drag (CD) and lift (CL). As the SC flows have fixed vortex separation points, vortex shedding is different from that in a single CC flow.

To show Reynolds-number dependence, the t–z averaged CL, CD, $(\nu_{sr})_{pm}$, their relevant RMS values CL$'$, CD$'$, $(\nu_{sr})'_p$, and St are given in Table 2 and illustrated in Figures 3a–3c. As shown in the third column of Table 2, for $\mathrm{Re}_3 = \mathrm{Re}/10^3 \in [5, 350]$, the mean CD is about 1.800($\pm$0.064), with

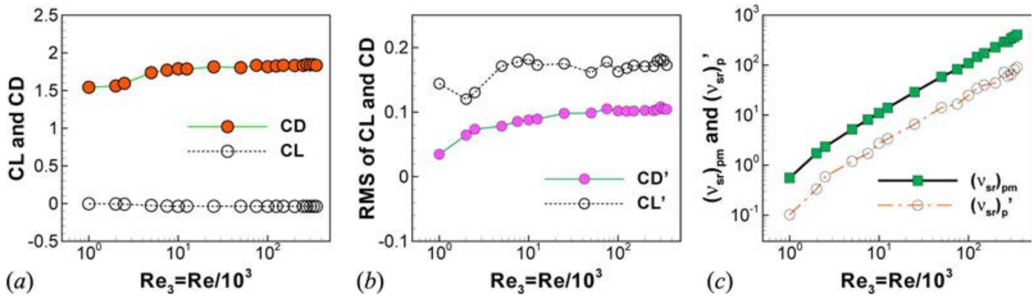

Figure 3. Re dependence of mean lift (CL) and drag (CD) (*a*), their root mean square (RMS) values of CL and CD (*b*), and the time-averaged viscosity ratio $(\nu_{sr})_{pm}$ as well as its relevant RMS $(\nu_{sr})'_p$ (*c*). Note that $(\nu_{sr})_{pm}$ is calculated merely by time-averaging for the peak value of $\nu_{sr}(=\nu_s/\nu)$ in the computational domain, as seen in Figure 6.

maximum relative deviation of 3.56%. This indicates that in the range of $Re_3 \in [5, 350]$, drag coefficient is Reynolds-number independent. For $Re_3 \in [1, 50]$, with the increase of Reynolds number, the mean CD increases gradually from 1.543 to 1.804. As indicated in the second column of Table 2, the mean CD is approximately zero. The Reynolds-number dependence of mean CD and CL is also shown in Figure 3*a*.

The Re dependence of relevant RMS values CL′, CD′, and $(\nu_{sr})'_p$ can be found from the fifth, sixth, and seventh columns of Table 2. The sub-grid viscosity is calculated from Eq. (1). Corresponding to the values given by the fifth and sixth columns of Table 2, the CL′ and CD′ are shown as functions of Re_3, as shown in Figure 3*b*. For $Re_3 \in [5, 350]$, CL′ is about $0.17(\pm 0.0117)$ with a maximum relative deviation of 6.88%; CD′ is around $0.1(\pm 0.0219)$.

It can be seen that values of the mean CD and its RMS values agree well with existing experimental data of Luo et al. [14] and LES results of Sohankar [34], although the RMS value of CL is less well predicted. The present LES results indicate that the CL′ value is about twice the CD′ value. Considering the wind tunnel measurement of Tamura and Miyagi [15], the effect of inlet turbulence on aerodynamic forces on a SC with various corner shapes indicates that the reason of the discrepancy requires further investigation.

The peak value of viscosity ratio (ν_{sr}) is sought from the entire computational domain, whose geometric parameters are shown in Table 1. As turbulent SC flow involves vortex shedding, the location point of the peak value changes temporally. The mean peak value of viscosity ratio $(\nu_{sr})_{pm}$ is based on t-averaging. From Figure 3*c*, it can be seen that Re dependence of $(\nu_{sr})_{pm}$ and its RMS value can be described by the power law, the $(\nu_{sr})_{pm}$ and its RMS value increase with Reynolds number, but the growing rate of $(\nu_{sr})_{pm}$ is larger. For instance, at $Re_3 = 125$, $(\nu_{sr})_{pm}$ is 146.23 with its RMS value of 34.14, as shown in Table 2.

As shown in Table 2, based on lift analysis with discrete Hilbert transform [94], for $Re_3 \in [1, 350]$, St is 0.1079 for all values of Re, with the power-spectra diagrams for $Re_3 = 1, 2, \ldots, 250$ and 350 given in Figures 4*a*–4*h*. This St number is close to the predicted St number of 0.124 for the case of $Re = 2.2 \times 10^4$ [19], when two-dimensional flow calculation was carried out based on the two-layer (TL) approach with standard $k-\varepsilon$ equation with inlet viscosity ratio $(r_\mu = \nu_t/\nu)$ set as 100. As reported by Bosch and Rodi [19], St number measured by Bearman and Trueman [8] was 0.123 for the SC flow at $Re \approx 5 \times 10^4$ when the inlet flow turbulence level $Tu(=\sqrt{u'^2})$ was less than 1.2%.

The relevant evolutions of CL and CD at Re_3=1, 2, …, and 325 are given in Figures 5*a*–5*h*. It can be seen that fluctuation of CD is less than that of CL, which is consistent with the CL′ and CD′ listed in the fifth and sixth columns of Table 2.

Some properties of the peak value of viscosity ratio can be seen in Figure 6. Both the mean peak value of viscosity ratio $(\nu_{sr})_{pm}$ and its RMS value have growing tendency, as shown in Figure 3*c*. The values of $(\nu_{sr})_{pm}$ as shown in Figure 6 are consistent with values shown in Table 2 for $Re_3 = 75$, 150, and 300.

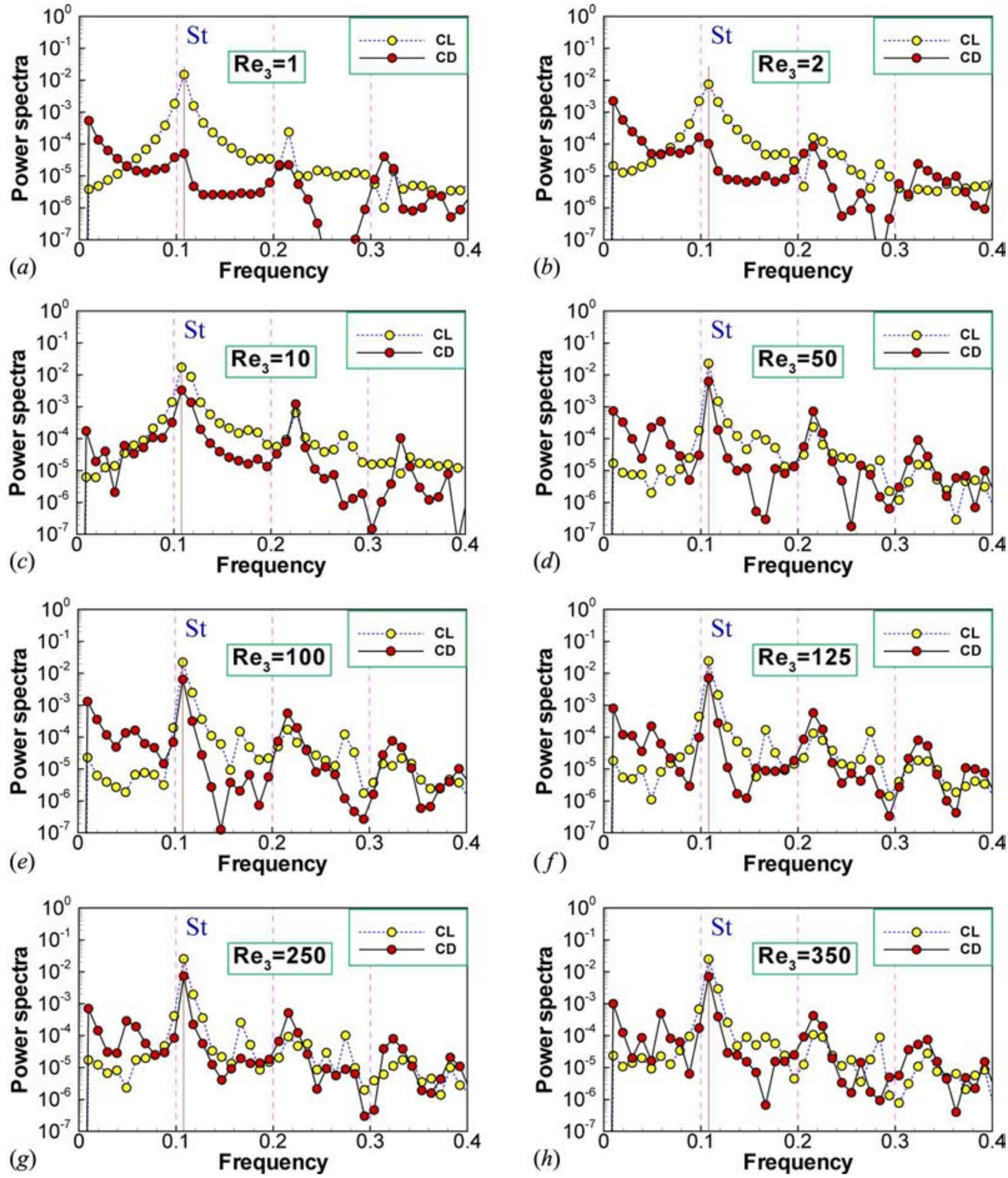

Figure 4. Power spectra of the evolutions of CD and CL at (*a*) $Re_3 = 1$; (*b*) $Re_3 = 2$; (*c*) $Re_3 = 10$; (*d*) $Re_3 = 50$; (*e*) $Re_3 = 100$; (*f*) $Re_3 = 125$; (*g*) $Re_3 = 250$; and (*h*) $Re_3 = 350$.

In Table 2, it can be seen that at $Re_3 = 50$, $CL' = 0.1612$, and $CD' = 0.0986$; while at $Re_3 = 125$, $CL' = 0.1679$, and $CD' = 0.1013$. In Figures 7*a*, *b*, it can be seen that the fluctuation magnitudes of CL and CD are approximately identical for the two cases $Re_3 = 50$, 125.

4.2. Fluid flow patterns

At $x = 3, 6, 9, 12$ and time $t = 170$, labeled by values -0.3, -0.2, -0.1, 0, 0.1, 0.2, and 0.3, the contours of streamwise vorticity component ω_1 for $Re_3 = 50$ are shown in Figures 8*a*–8*d*, with the relevant ω_1 contours for $Re_3 = 125$ shown in Figures 8*e*–8*h*. A comparison indicates that the secondary flow

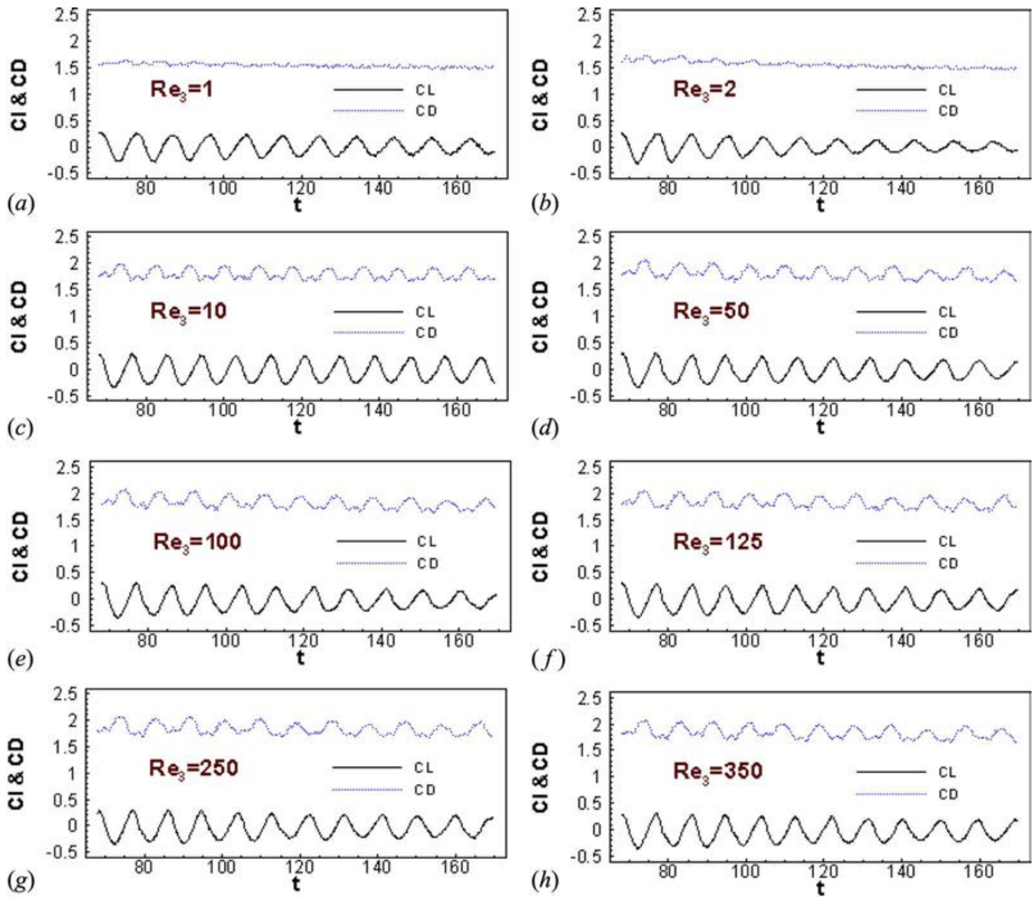

Figure 5. Evolutions of lift (CL) and drag (CD). (*a*) $Re_3 = Re/10^3 = 1$; (*b*) $Re_3 = 2$; (*c*) $Re_3 = 10$; (*d*) $Re_3 = 50$; (*e*) $Re_3=100$; (*f*) $Re_3 = 125$; (*g*) $Re_3 = 250$; and (*h*) $Re_3 = 350$.

patterns are Re dependent. Similarly, the main stream flow patterns given by contours of ω_3 are shown in Figures 9*a*, *b*.

4.3. t–z averaged variable distributions

Even though the peak value of viscosity ratio $(\nu_{sr})_{pm}$ varies as a result of large eddy motion in the flow field, exploring the occurrence of peak value is helpful to the understanding of the characteristics of the SC flows. For $Re_3 = 50$ and 125, the *t*–*z* averaged viscosity ratios ν_{sr} are shown by the contours

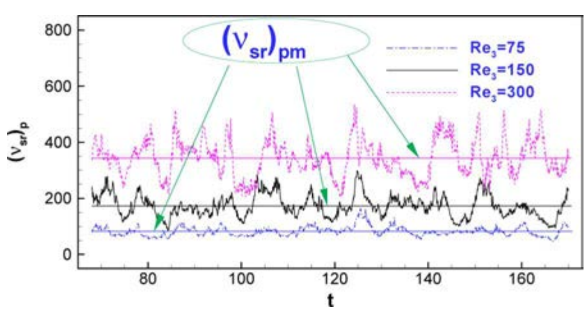

Figure 6. Evolutions of the peak value of viscosity ratio ($(\nu_{sr})_p \equiv (\nu_s/\nu)_{peak}$) at $Re_3 = 75$, 150, and 300.

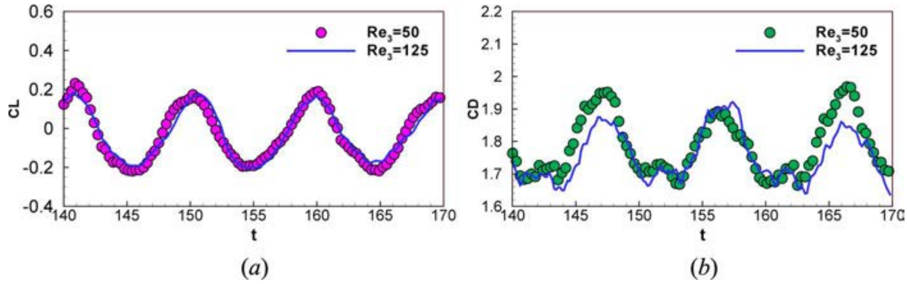

Figure 7. Evolutions of lift (CL) (*a*) and drag (CD) (*b*) coefficients at $Re_3 = 50$ and 125.

labeled as 0.05, 1, 5, and 10 in Figures 10*a*, *b*. The red colored zone corresponds to the *t*–*z* averaged viscosity ratio $\nu_{sr} \geq 10$, the blue colored region corresponds to $\nu_{sr} \leq 0.05$, whereas the yellow, green, and cyan colored regions refer to the ranges of $\nu_{sr} \in (5, 10)$, (1, 5), and (0.05, 1). As shown in Figures 10*a*, *b*, for $Re_3 = 50$, and 125, the peak of viscosity ratio occurs in two downstream regions, where the coherent interaction of large eddies is more intense.

For turbulent SC flows, Kolmogorov micro-scale is predicted on the basis of estimating the kinetic energy dissipation rate, similar to previous work [52, 65]. Denoting the Taylor micro-scale as λ_u [95], we have

$$\lambda_u^2 = 10\nu k/\varepsilon, \quad \eta_u^2 = \left(\nu^2/\varepsilon\right)^{1/2} = \lambda_u^2\left[\nu(\varepsilon/\nu)^{1/2}/(10\ k)\right] \tag{24}$$

where $k = \frac{1}{2}\overline{u_i'^2}$ is the time and *z*-averaged turbulent kinetic energy, u_i' is the instantaneous fluctuation of velocity component in the x_i-direction. While ε is the dissipation rate of k

$$\varepsilon = 2\nu\overline{s_{ij}s_{ij}}, \quad s_{ij} = (\partial u_i'/\partial x_j + \partial u_j'/\partial x_i)/2 \tag{25}$$

with s_{ij} being the fluctuation of strain rate of velocity field.

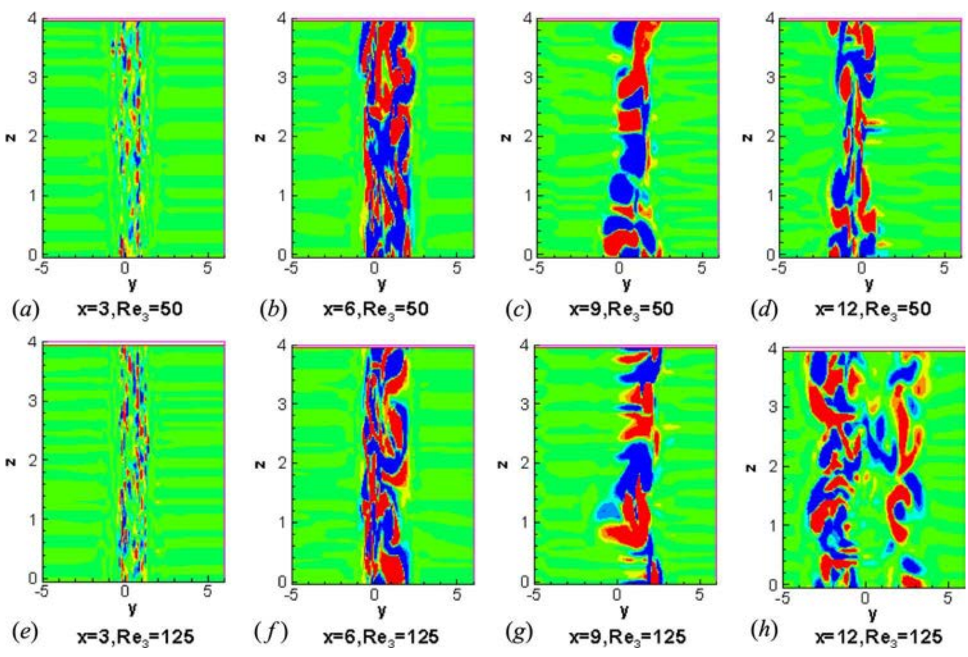

Figure 8. Contours of streamwise vorticity component (ω_1) at $t = 170$, and four x-locations (i.e., x=3, 6, 9, and 12) for $Re_3 = 50$ (*a*–*d*) and $Re_3 = 125$ (*e*–*h*). Note that the contours are labeled by −0.3, −0.2, −0.1, 0, 0.1, 0.2, and 0.3.

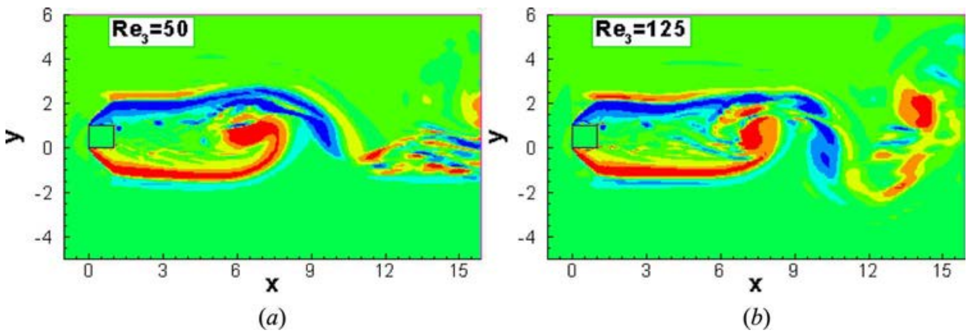

Figure 9. Contours of spanwise vorticity component (ω_3) at $t = 170$ and $z = 2$ for $Re_3 = 50$ (*a*) and $Re_3=125$ (*b*). Note that contours of ω_3 are labeled by -2, -1, -0.5, 0, 0.5, 1, and 2.

The t–z averaged field of Kolmogorov micro-scale [log (η_u)] is shown in Figures 11*a*, *b* for two Reynolds numbers $Re_3 = 50$ and 125. The t–z averaged Kolmogorov micro-scale [log (η_u)] is less than -3 for blue colored region, but larger than -2.7 for red colored region. The yellow, green, and cyan colored regions correspond to log (η_u) $\in (-3, -2.9)$, $(-2.9, -2.8)$, and $(-2.8, -2.7)$.

From Figures 11*a*, *b*, it can be seen that in the near SC wall regions log (η_u) is less than -3. With respect to the definition of η_u given by Eq. (24), this property of log (η_u) distribution indicates that near the SC, the dissipation rate of turbulent kinetic energy is larger because of the fluid–solid interaction. From Figures 11*a*, *b*, there is an asymmetry of distribution of log (η_u), suggesting that in the SC flow the vortex shedding from the two fix points is not equivalent, which may lead to an asymmetrical distribution of k and its dissipation rate ε [96].

4.4. Instantaneous iso-surfaces

The iso-surfaces of FSI at $t = 170$ in the sub-domain $\{x \in (0, 7), y \in (-2, 3), z \in (1, 3)\}$ are shown in Figures 12*a*, *c*. As seen in Eq. (2), the iso-surfaces of FSI depend on vortex motion, which can be quantified by swirling-strength λ_{ci} [69–71]. The FSI has a laminated structure involving vortex shedding, in addition to those relatively small vortex structures in the SC wake. The distribution of FSI iso-surfaces is Re dependent, since the FSI iso-surfaces as shown in Figure 12*a* have some differences from those shown by Figure 12*c*.

The iso-surfaces of viscosity ratio ν_{sr} are shown in Figures 12*b*, *d*, indicating the reliability of t–z averaged distribution as given in Figures 11*a*, *b*.

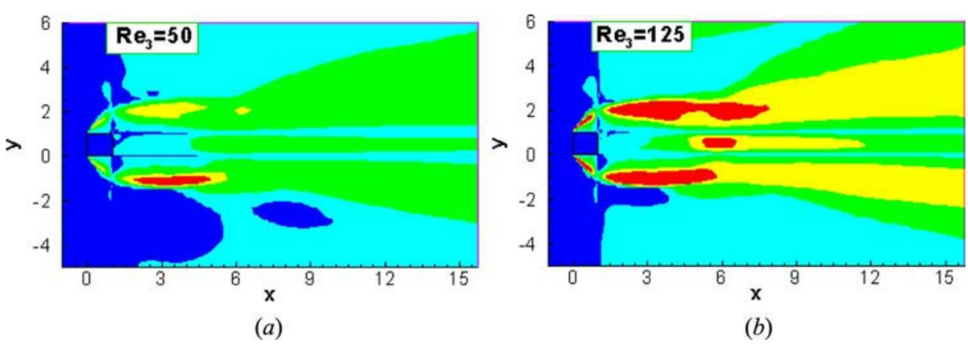

Figure 10. Contours of the (t–z) averaged sub-grid viscosity ratio (ν_{sr}) at $Re_3 = 50$ (*a*) and 125 (*b*). Note that the contours of ν_{sr} are labeled by 0.05, 1, 5, and 10.

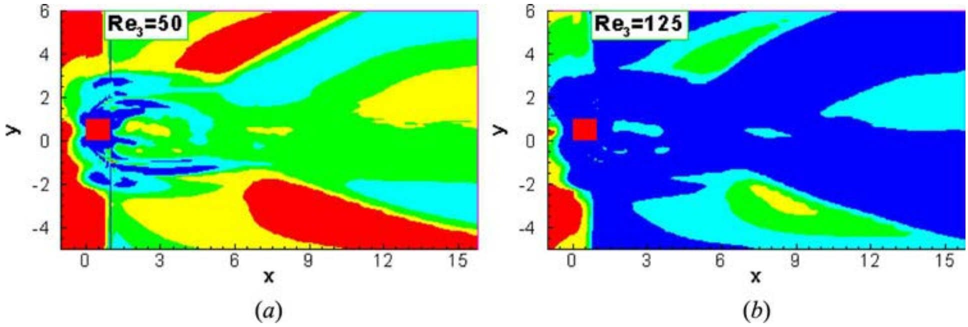

Figure 11. Contours of the (*t*–*z*) averaged logarithm of Kolmogorov micro-scale to the base of 10 [log(η_u)] at $Re_3 = 50$ (*a*) and 125 (*b*). Note that the contours of log(η_u) are labeled by −3, −2.9, −2.8, and −2.7.

4.5. Nusselt numbers

The Re dependence of time-face averaged Nusselt numbers and their arithmetic mean are given in Table 3, with the relevant RMS values shown in Table 4. These Nusselt numbers are based on the length scale *d*, as shown in Figures 13*a*, *b*. Figure 13*a* shows that the frontal face averaged Nusselt number Nu_f is rather sensitive to Re, having the largest growing rate. This is mainly caused by the impingement of free flow stream. While the growing rates of bottom, top, and rear face averaged Nusselt numbers, Nu_b, Nu_t, and Nu_r are smaller, and comparable to each other, primarily caused by the SC flows at zero incident angle have fixed separation points. Influenced by the recirculation near the rear face, the RMS value Nu_r' is larger than other RMS values, see in Table 4 or Figure 13*b*.

Following the comparison approach of Wiesche [4], we further choose 2*d* as the length scale for the arithmetic mean Nusselt number calculation. In comparing, respectively, with empirical correlations of Hilpert [2] and Igarashi [3], the Re dependence of Nu_{2d} and the corresponding relative deviations

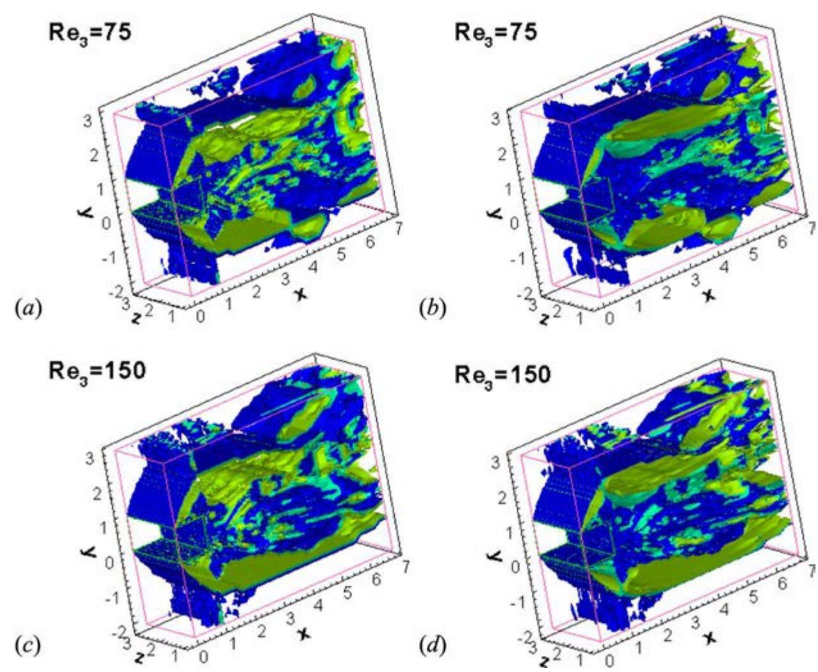

Figure 12. Iso-surfaces of factor of swirling-strength intermittency (FSI) at $t = 170$ for $Re_3 = 75$ (*a*) and $Re_3 = 150$ (*c*); iso-surfaces of sub-grid viscosity ratio (ν_{sr}) at $t = 170$ for $Re_3 = 75$ (*b*) and Re_3=150 (*d*). Note that the SC is illustrated simply by a yellow cylinder frame; the FSI iso-surfaces are labeled by 0.05, 0.5, and 0.95, with ν_{sr} iso-surfaces labeled by 0.05, 1, and 5.

Table 3. Re dependence of Nusselt numbers.

Re_3	Nu_b	Nu_t	Nu_f	Nu_r	Nu_m^a
1	4.941	5.180	21.38	2.416	8.477
2	5.709	6.228	30.28	3.454	11.42
2.5	6.068	6.789	34.08	4.155	12.77
5	7.928	9.625	49.52	7.281	18.59
7.5	9.647	11.874	62.09	9.746	23.34
10	11.28	14.02	73.10	12.03	27.61
12.5	12.81	15.98	84.32	14.33	31.86
25	21.31	24.86	130.41	21.97	49.64
50	33.69	40.41	203.15	36.66	78.48
75	46.57	53.87	263.45	53.99	104.47
100	55.98	65.61	309.14	61.68	123.09
125	65.03	79.04	356.69	73.97	143.68
150	72.79	89.86	405.63	85.21	163.37
200	89.45	111.66	508.36	114.43	205.97
250	100.36	127.41	623.69	142.75	248.55
275	107.02	139.74	690.60	162.30	274.91
300	113.17	148.76	764.71	175.91	300.64
325	117.09	154.58	878.87	192.40	335.73
350	118.77	158.32	1134.57	197.64	402.32

[a]The arithmetic mean Nusselt number, $Nu_m = (Nu_b + Nu_t + Nu_f + Nu_r)/4$.

Table 4. Re dependence of the RMS values of Nusselt numbers.

Re_3	Nu'_b	Nu'_t	Nu'_f	Nu'_r	Nu'_m
1	0.2076	0.3650	0.0868	0.2670	0.1250
2	0.1874	0.4965	0.2407	0.5667	0.2795
2.5	0.1875	0.6016	0.2838	0.7099	0.3802
5	0.3304	0.5897	0.3082	0.8985	0.4657
7.5	0.6190	0.646	0.3962	1.117	0.4568
10	0.9046	0.9851	0.4588	1.383	0.4224
12.5	1.172	1.364	0.583	1.525	0.4680
25	2.136	2.687	1.160	4.029	1.379
50	4.743	5.191	1.881	8.715	3.734
75	7.163	7.541	1.911	13.63	5.486
100	9.488	10.46	2.616	17.33	7.575
125	11.56	12.66	3.04	20.86	8.84
150	13.34	15.66	3.51	25.29	10.16
200	17.61	22.20	4.92	62.71	20.30
250	18.30	42.65	7.18	93.93	32.37
275	19.53	49.19	8.67	113.78	37.85
300	20.07	53.48	12.66	120.66	40.39
325	21.71	55.67	34.69	139.73	47.20
350	25.66	60.95	65.24	147.66	50.02

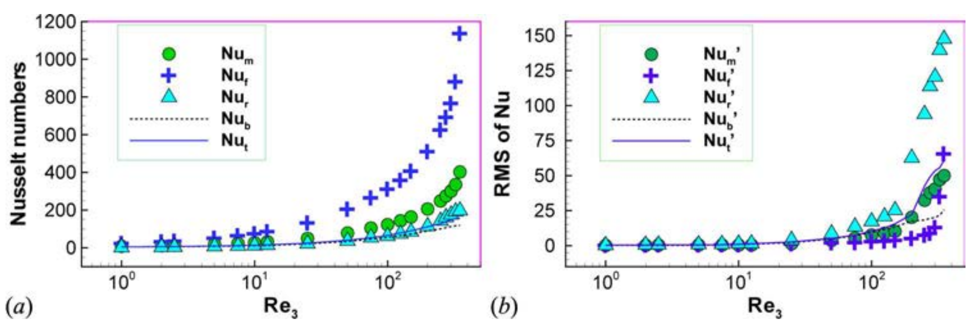

Figure 13. Re dependence of Nusselt numbers and their RMS values. Note that here *d* is used as the length scale to define these Nusselt numbers.

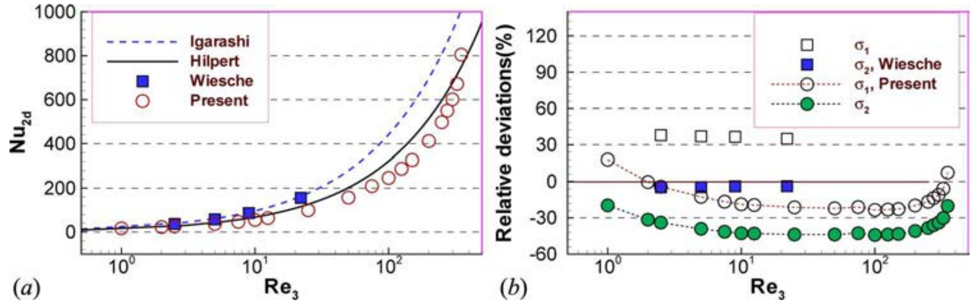

Figure 14. Re dependence of Nu_{2d} and the relevant relative deviations σ_1 and σ_2. Note that $\sigma_1 = (Nu_{2d} - Nu_{exp1})/Nu_{exp1} \times 100\%$, $\sigma_2 = (Nu_{2d} - Nu_{exp2})/Nu_{exp2} \times 100\%$, where for $Re_{2d} = 2Re$, $Nu_{exp1} = 0.085Re_{2d}^{0.675}$ in Ref. [2]; $Nu_{exp2} = 0.14Re_{2d}^{0.66}$ in Ref. [3].

(σ_1, σ_2) are shown in Figures 14*a*, *b*. It can be seen that the present LES has predicted the mean Nusselt numbers which are consistent with the empirical correlation obtained by earlier experiments of Hilpert [2].

According to the review of Sparrow et al. [5], the change of length scale is to some extent inappropriate. For the SC wake flows at incident angle, the length scale for Nusselt numbers should be the SC's sectional side length *d*. The present LES has predicted the mean Nusselt number in good agreement with the correlation of Hilpert [2]. Igarashi [3] utilized constant *heat flux* in the wind tunnel measurement, resulting in higher values of mean Nusselt number in comparison with those under isothermal wall temperature [97].

5. Conclusions

A swirling-strength based SGS (SbSGS) model is used in the LES of zero-incident incompressible turbulent flows around a SC with convective heat transfer at Reynolds numbers ranging from 10^3 to 3.5×10^5. LES is performed by a finite difference method, where Taylor-expansion is used to improve the accuracy of discretization. It reveals the following:

1. For Reynolds numbers in the range of 10^3 to 3.5×10^5, Strouhal number is 0.1079, independent of Reynolds number.
2. Mean drag coefficient CD is about 1.800($\pm$0.064) when $Re \geq 5000$, with a maximum relative deviation of 3.56%.
3. The peak value of sub-grid viscosity ratio and its RMS values increase with Reynolds number. The peak occurs in two regions downstream of the SC, when the coherent interactions of large eddies are more intensive.
4. Kolmogorov micro-scale is less than 10^{-3} in the near SC wall region when the Reynolds number is over 7.5×10^4. The larger the Reynolds number, the smaller is the Kolmogorov micro-scale.
5. The time-averaged Nusselt number at the frontal face increases with Re rapidly due to the free flow stream impingement. While the RMS at the rear face is larger than other RMS values.

Funding

This work was supported by the Research Committee of The Hong Kong Polytechnic University (Grant No. G-YL03 and G-YM37) and NSFC (11372303).

References

[1] Z. J. Zhu, *Numerical Study of Flows Around Rectangular Cylinders*, Ph.D. thesis, Shanghai Jiaotong University, P.R. China, pp. 1–22, 1990 (in Chinese).

[2] R. Hilpert, Wärmeabgabe von beheizten Dräten und Rohren im Luftstrom. Forsch. Ingenieurwesen, vol. 4, pp. 215–224, 1933; also: E. Eckert, *Einführung in den Wärme- und Stoffaustausch*, Springer, Berlin Heidelberg, New York, 1959.
[3] T. Igarashi, Fluid Flow and Heat Transfer Around Rectangular Cylinders (The Case of a Width/Height Ratio of a Section of 0.33–1.5), *Int. J. Heat Mass Transfer*, vol. 30, pp. 893–901, 1987.
[4] S. aus der Wiesche, Large-Eddy Simulation Study of an Air Flow Past a Heated Square Cylinder, *Heat Mass Transfer*, vol. 43, pp. 515–525, 2007.
[5] E. M. Sparrow, J. P. Abraham, and H. C. K. Tong, Archival Correlations for Average Heat Transfer Coefficients for Non-Circular Cylinders and for Spheres in Cross-Flow, *Int. J. Heat Mass Transfer*, vol. 47, pp. 5285–5296, 2004.
[6] B. J. Vickery, Fluctuating Lift and Drag on a Long Cylinder of Square Cross-Section in a Smooth and in a Turbulent Stream, *J. Fluid Mech.*, vol. 25, pp. 481–494, 1966.
[7] A. Okajima, Strouhal Numbers of Rectangular Cylinders, *J. Fluid Mech.*, vol. 123, pp. 379–398, 1982.
[8] P. W. Bearman and D. M. Trueman, An Investigation of the Flow Around Rectangular Cylinders, *Aeronaut. Q.*, vol. 23, pp. 229–237, 1972.
[9] J. Courchesne and A. Laneville, An Experimental Evaluation of Drag Coefficient for Rectangular Cylinders Exposed to Grid Turbulence, *ASME J. Fluids Eng.*, vol. 104, pp. 523–528, 1982.
[10] Y. Nakamura and Y. Tomonari, The Effect of Turbulence on the Drags of Rectangular Prisms, *Jpn. Soc. Aeronaut. Space Sci. Trans.*, vol. 19, pp. 82–86, 1976.
[11] R. W. Davis, E. F. Moore, and L. P. Purtell, A Numerical-Experimental Study on Confined Flow Around Rectangular Cylinders, *Phys. Fluids*, vol. 23, pp. 46–59, 1984.
[12] D. A. Lyn and W. Rodi, The Flapping Shear Layer Formed by Flow Separation from the Forward Corner of a Square Cylinder, *J. Fluid Mech.*, vol. 267, pp. 353–376, 1994.
[13] J. C. K. Tong, J. P. Abraham, J. M. Y. Tse, and E. M. Sparrow, Using Corner Chamfers to Reduce the Drag of Flat-Sided Columns, *Proc. ICE – Eng. Comput. Mech.*, vol. 168, no. 2, pp. 79–88, 2015.
[14] S. C. Luo, M. G. Yazdani, Y. T. Chew, and T. S. Lee, Effects of Incidence and Afterbody Shape on Flow Past Bluff Cylinders, *J. Wind Eng. Ind. Aerodynam.*, vol. 53, pp. 375–99, 1994.
[15] T. Tamura and T. Miyagi, The Effect of Turbulence on Aerodynamic Forces on a Square Cylinder with Various Corner Shapes, *J. Wind Eng. Ind. Aerodynam.*, vol. 83, pp. 135–145, 1999.
[16] S. C. Luo, Y. T. Chew, and Y. T. Ng, Characteristics of Square Cylinder Wake Transition Flows, *Phys. Fluids*, vol. 15, pp. 2549–2559, 2003.
[17] A. K. Saha, K. Muralidhar, and G. Biswas, Experimental Study of Flow Past a Square Cylinder at High Reynolds Numbers, *Exp. Fluids*, vol. 29, nos. 1–6, pp. 553–563, 2000.
[18] H. F. Wang and Y. Zhou, The Finite-Length Square Cylinder Near Wake, *J. Fluid Mech.*, vol. 638, pp. 453–490, 2009.
[19] G. Bosch and W. Rodi, Simulation of Vortex Shedding Past a Square Cylinder with Different Turbulence Models, *Int. J. Numer. Meth. Fluids*, vol. 28, pp. 601–616, 1998.
[20] M. Kato and B. E. Launder, The Modelling of Turbulent Flow Around Stationary and Vibrating Square Cylinders, Proc. 9th Symp. Turbulent Shear Flows, Kyoto, 10–4-1, 1993.
[21] K. Ryu, S. J. Yook, and K. S. Lee, Forced Convection Across a Locally Heated Square Cylinder Near a Wall, *Numer. Heat Transfer, A: Appl.*, vol. 66, no. 10, pp. 972–986, 2014.
[22] J. L. Niu, Z. J. Zhu, and S. H. Huang, Numerical Study of Convective Heat Transfer from Two Identical Square Cylinders Submerged in a Uniform Cross Flow, *Numer. Heat Transfer, A: Appl.*, vol. 50, pp. 21–44, 2006.
[23] J. L. Niu and Z. J. Zhu, Numerical Study of Three-Dimensional Flows Around Two Identical Square Cylinders in Staggered Arrangements, *Phys. Fluids*, vol. 18, p. 044106, 2006.
[24] A. Sohankar, C. Norberg, and L. Davidson, Simulation of Three-Dimensional Flow Around a Square Cylinder at Moderate Reynolds Numbers, *Phys. Fluids*, vol. 11, pp. 288–306, 1999.
[25] A. K. Saha, G. Biswas, and K. Muralidhar, Three-Dimensional Study of Flow Past a Square Cylinder at Low Reynolds Numbers, *Int. J. Heat Fluid Flow*, vol. 24, pp. 54–66, 2003.
[26] A. K. Saha, K. Muralidhar, and G. Biswas, Vortex Structures and Kinetic Energy Budget in Two-Dimensional Flow Past a Square Cylinder, *Comput. Fluids*, vol. 29, no. 6, pp. 669–694, 2000.
[27] A. K. Saha, K. Muralidhar, and G. Biswas, Transition and Chaos in Two-Dimensional Flow Past a Square Cylinder, *ASCE J. Eng. Mech.*, vol. 126, no. 5, pp. 523–532, 2000.
[28] D. Chatterjee, G. Biswas, and S. Amiroudine, Mixed Convection Heat Transfer from a in Line Row of Square Cylinders in Cross Flow at Low Reynolds Number, *Numer. Heat Transfer, A: Appl.*, vol. 61, no. 12, pp. 891–911, 2012.
[29] D. Chatterjee and B. Mondal, Mixed Convection Heat Transfer from Tandem Square Cylinder for Various Gap to Size Ratios, *Numer. Heat Transfer, A: Appl.*, vol. 62, no. 2, pp. 101–119, 2013.
[30] F. Karimi, H. T. Xu, Z. Wang, M. Yang, and Y. Zhang, Numerical Simulation of Unsteady Convection from Heated Horizontal Circular Cylinders in a Square Enclosure, *Numer. Heat Transfer, A: Appl.*, vol. 65, no. 8, pp. 715–731, 2014.

[31] D. Chatterjee and S. K. Gupta, Convective Transport Around a Rotating Square Cylinder at Moderate Reynolds Numbers, *Numer. Heat Transfer, A: Appl.*, vol. 67, no. 12, pp. 1386–1407, 2015.
[32] D. Chatterjee and S. K. Gupta, Convective Transport Around Rows of Square Cylinders in Staggered Fashion at Moderate Reynolds Numbers, *Numer. Heat Transfer, A: Appl.*, vol. 68, no. 4, pp. 388–410, 2015.
[33] S. Krajnovic and L. Davidson, Large Eddy Simulation of the Flow Around a Bluff Body, *AIAA J.*, vol. 40, no. 5, pp. 927–936, 2002.
[34] A. Sohankar, Flow over a Bluff Body from Moderate to High Reynolds Numbers using Large Eddy Simulation, *Comput. Fluids*, vol. 35, pp. 1154–1168, 2006.
[35] K. Hanjalic, One-Point Closure Model for Buoyancy-Driven Turbulent Flows, *Annu. Rev. Fluid Mech.*, vol. 34, pp. 321–347, 2002.
[36] N. N. Smirnov and V. F. Nikitin, Modeling and Simulation of Hydrogen Combustion in Engines, *Int. J. Hydrogen Energy*, vol. 112, pp. 1122–1136, 2014.
[37] P. Holmes, J. L. Lumley, and G. Berkooz, *Turbulence, Coherent Structures, Dynamical Systems and Symmetry*, Cambridge University Press, Cambridge, 1996.
[38] J. S. Smagorinsky, Gesneral Circulation Experiments with the Primitive Equations, the Basic Experiment, *Mon. Weather Rev.*, vol. 91, no. 3, pp. 99–164, 1963.
[39] P. Moin and J. Kim, Numerical Investigation of Turbulent Channel Flow, *J. Fluid Mech.*, vol. 118, pp. 341–377, 1982.
[40] M. S. Vázquez and O. Métais, Large-Eddy Simulation of the Turbulent Flow through a Heated Square Duct, *J. Fluid Mech.*, vol. 453, pp. 201–238, 2002.
[41] O. Métais and M. Lesieur, New Tren in Large Eddy Simulation of Turbulence, *Annu. Rev. Fluid Mech.*, vol. 28, pp. 45–82, 1996.
[42] J. Pallares and L. Davidson, Large-Eddy Simulations of Turbulent Flow in a Rotating Square Duct, *Phys. Fluids*, vol. 12, pp. 2878–2894, 2000.
[43] K. F. Yu, K. S. Lau, and C. K. Chan, Large Eddy Simulation of Particle-Laden Turbulent Flow over a Backward-Facing Step, *Commun. Nonlinear Sci. Numer. Simul.*, vol. 9, no. 2, pp. 251–262, 2004.
[44] Y. C. Guo, P. Jiang, C. K. Chan, and W. Y. Lin, Large Eddy Simulation of Coherent Structures in Rectangular Methane Non-Premixed Flame, *J. Comput. Appl. Math.*, vol. 235, no. 13, pp. 3760–3767, 2011.
[45] C. Duwig, K. J. Nogenmyr, C. K. Chan, and M. Dunn, Large Eddy Simulations of a Piloted Lean Premixed Jet Flame using Finite-Rate Chemistry, *Combust., Theory Modell.*, vol. 15, no. 4, pp. 537–568, 2011.
[46] Y. Y. Wu, C. K. Chan, and L. X. Zhou, Large Eddy Simulation of an Ethylene-Air Turbulent Premixed v-Flame, *J. Comput. Appl. Math.*, vol. 235, no. 13, pp. 3768–3774, 2011.
[47] M. Germano, U. Piomelli, P. Moin, and W. H. Cabot, A Dynamic Subgrid-Scale Eddy Viscosity Model, *Phys. Fluids A*, vol. 3, no. 7, pp. 1760–1765, 1991.
[48] D. K. Lilly, A Proposed Modification of the Germano Subgrid-Scale Closure Model, *Phys. Fluids A*, vol. 4, no. 3, pp. 633–635, 1992.
[49] G. X. Cui, C. X. Xu, and Z. S. Zhang, Progress in Large Eddy Simulation of Turbulent Flows, *Acta Aerodynam. Sin.*, vol. 22, no. 2, pp. 121–129, 2004 (in Chinese).
[50] G. X. Cui, H. B. Zhou, Z. S. Zhang, and L. Shao, A New Subgrid Eddy Viscosity Model and Its Application, *Chin. J. Comput. Phys.*, vol. 21, no. 3, pp. 289–293, 2004 (in Chinese).
[51] A. W. Vreman, An Eddy-Viscosity Subgrid-Scale Model for Turbulent Shear Flow: Algebraic Theory and Applications, *Phys. Fluids*, vol. 16, no. 10, pp. 3670–3681, 2004.
[52] Z. J. Zhu, H. X. Yang, and T. Y. Chen, Numerical Study of Turbulent Heat and Fluid Flow in a Straight Square Duct at Higher Reynolds Numbers, *Int. J. Heat Mass Transfer*, vol. 53, pp. 356–364, 2010.
[53] F. Nicoud, H. B. Toda, O. Cabrit, S. Bose, and J. Lee, Using Singular Values to Build a Subgrid-Scale Model for Large Eddy Simulations, *Phys. Fluids*, vol. 23, p. 085106, 2011.
[54] A. Verma and K. Mahesh, A Lagrangian Subgrid-Scale Model with Dynamic Estimation of Lagrangian Time Scale for Large Eddy Simulation of Complex Flows, *Phys. Fluids*, vol. 24, p. 085101, 2012.
[55] D. D. Holm, Fluctuation Effects on 3d Lagrangian Mean and Eulerian Mean Fluid Motion, *Phys. D*, vol. 133, nos. 1–4, pp. 215–269, 1999.
[56] A. Cheskidov, D. D. Holm, E. Olson, and E. S. Titi, On a Leray- Model of Turbulence, *Proc. Roy. Soc. Lond. A*, vol. 461, no. 2055, pp. 629–649, 2005.
[57] B. J. Geurts and D. D. Holm, Regularization Modeling for Large-Eddy Simulation, *Phys. Fluids*, vol. 15, pp. L13–L16, 2003.
[58] M. van Reeuwijk, H. J. J. Jonker, and K. Hanjalic, Wind and Boundary Layers in Rayleigh Bernard Convection. *I. Analysis and Modelling, Phys. Rev. E*, vol. 77, p. 036311, 2008.
[59] M. van Reeuwijk, H. J. J. Jonker, and K. Hanjalic, Leray- Simulations of Wall-Bounded Turbulent Flows, *Int. J. Heat Fluid Flow*, vol. 30, pp. 1044–1053, 2009.
[60] E. Tadmor, Convergence of Spectral Methods for Nonlinear Conservation Laws, *SIAM J. Numer. Anal.*, vol. 26, pp. 1–30, 1989.

[61] G. Karamanos and G. E. Karniadakis, A Spectral Vanishing Viscosity Method for Large-Eddy Simulations, *J. Comput. Phys.*, vol. 163, pp. 22–50, 2000.
[62] R. Pasquetti, Spectral Vanishing Viscosity Method for Large-Eddy Simulation of Turbulent Flows, *J. Sci. Comput.*, vol. 27, pp. 365–375, 2006.
[63] E. Lamballais, V. Fortuné, and S. Laizet, Straightforward High-Order Numerical Dissipation via the Viscous Term for Direct and Large Eddy Simulation, *J. Comput. Phys.*, vol. 230, pp. 3270–3275, 2011.
[64] T. Dairay, V. Fortuné, E. Lamballais, and L. E. Brizzi, LES of a Turbulent Jet Impinging on a Heated Wall using High-Order Numerical Schemes, *Int. J. Heat Fluid Flow*, vol. 50, pp. 177–187, 2014.
[65] Z. J. Zhu, J. L. Niu, and Y. L. Li, Swirling-Strength based Large Eddy Simulation of Turbulent Flows Around Single Square Cylinder at Low Reynolds Numbers, *Appl. Math. Mech. Engl. Ed.*, vol. 35, pp. 959–978, 2014.
[66] Z. Zhang, W. Chen, Z. J. Zhu, and Y. L. Li, Numerical Exploration of Turbulent Natural-Convection in a DASC (i.e., Differentially-Heated Air-Filled Square Cavity) at $Ra = 5.33\times10^9$, *Heat Mass Transfer*, vol. 50, pp. 1737–1749, 2014.
[67] N. Uddin, S. O. Neumann, B. Weigand, and B. A. Younis, Large Eddy Simulation and Heat Flux Modeling in a Turbulent Impinging Jet, *Numer. Heat Transfer, A: Appl.*, vol. 55, pp. 906–930, 2009.
[68] S. Chandrasekhar, *Hydrodynamic and Hydromagnetic Stability, Chap. III*, Oxford University Press, Cambridge, 1961.
[69] J. Zhou, R. J. Adrian, S. Balachandar, and T. M. Kendall, Mechanisms of Generating Coherent Packets of Hairpin Vortices in Channel Flow, *J. Fluid Mech.*, vol. 387, pp. 353–396, 1999.
[70] B. Ganapathisubramani, E. K. Longmire, and I. Marusic, Experimental Investigation of Vortex Properties in a Turbulent Boundary Layer, *Phys. Fluids*, vol. 18, p. 155105, 2006.
[71] C. T. Lin and Z. J. Zhu, Direct Numerical Simulation of Incompressible Flows in a Zero-Pressure Gradient Turbulent Boundary Layer, *Adv. Appl. Math. Mech.*, vol. 2, pp. 503–517, 2010.
[72] D. K. Lilly, The Representation of Small-Scale Turbulence in Numerical Simulation Experiments, in H. H. Goldstine (ed.), *Proc. of IBM Scientific Computing Symposium on Environmental Sciences, Yorktown Heights*, New York, pp. 195–210, 1967.
[73] I. Orlanski, A Simple Boundary Condition for Unbounded Flows, *J. Comput. Phys.*, vol. 21, pp. 251–269, 1976.
[74] H. X. Yang, T. Y. Chen, and Z. J. Zhu, Numerical Study of Forced Turbulent Heat Convection in a Straight Square Duct, *Int. J. Heat Mass Transfer*, vol. 52, pp. 3128–3136, 2009.
[75] W. Q. Tao, *Numerical Heat Transfer*, Xi'an Jiantong University Press, P.R. China, pp. 195–251, 2001 (in Chinese).
[76] S. V. Patankar, *Numerical Heat Transfer and Fluid Flow*, Hemisphere, New York, 1980.
[77] F. H. Harlow and J. E. Welch, Numerical Calculation of Time Dependent Viscous Incompressible flow of Fluid with Free Surfaces, *Phys. Fluids*, vol. 8, pp. 2182–2188, 1965.
[78] G. Groetzbach, Direct Numerical Simulation of Laminar and Turbulent Benard Convection, *J. Fluid Mech.*, vol. 119, pp. 27–53, 1982.
[79] M. Manhart, A Zonal Grid Algorithm for DNS of Turbulent Boundary Layers, *Comput. Fluids*, vol. 33, pp. 435–461, 2004.
[80] K. Khanafer, K. Vafai, and M. Lightstone, Mixed Convection Heat Transfer in Two Dimensional Open-Ended Enclosures, *Int. J. Heat Mass Transfer*, vol. 45, pp. 5171–5190, 2002.
[81] E. Papanicolaou and Y. Jaluria, Transition to a Periodic Regime in Mixed Convection in a Square Cavity, *J. Fluid Mech.*, vol. 239, pp. 489–509, 1992.
[82] N. Nikitin, Finite-Difference Method for Incompressible Navier-Stokes Equations in Arbitrary Orthogonal Curvilinear Coordinates, *J. Comput. Phys.*, vol. 217, pp. 759–781, 2006.
[83] M. J. Ni and M. A. Abdou, A Bridge between Projection Methods and Simple Type Methods for Incompressible Navier-Stokes Equations, *Int. J. Numer. Meth. Eng.*, vol. 72, pp. 1490–1512, 2007.
[84] Z. F. Tian, X. Liang, and P. X. Yu, A Higher Order Compact Finite Difference Algorithm for Solving the Incompressible Navier-Stokes Equations, *Int. J. Numer. Meth. Eng.*, vol. 88, pp. 511–532, 2011.
[85] M. ElAbdallaoui, M. Hasnaoui, and A. Amahmid, Lattice-Bolzmann Modeling of Natural Convection between a Square Outer Cylinder, and an Inner Isoscales Triangular Heating Body, *Numer. Heat Transfer, A: Appl.*, vol. 66, no. 9, pp. 1076–1096, 2014.
[86] Z. Wang, Z. Huang, W. Zhang, and G. Xi, A Multidomain Chebyshev Pseudo-Spectral Method for Fluid Flow, and Heat Transfer from Square Cylinders, *Numer. Heat Transfer, B: Fundam.*, vol. 68, no. 3, pp. 224–238, 2015.
[87] F. X. Trias, A. Gorobets, and A. Oliva, A Simple Approach to Discretize the Viscous Terms with Spatially Varying (Eddy-) Viscosity, *J. Comput. Phys.*, vol. 253, pp. 405–417, 2013.
[88] D. L. Brown, R. Cortez, and M. L. Minion, Accurate Projection Methods for the Incompressible Navier-Stokes Equations, *J. Comput. Phys.*, vol. 168, pp. 464–499, 2001.
[89] Z. J. Zhu and H. X. Yang, Numerical Investigation of Transient Laminar Natural Convection of Air in a Tall Cavity, *Heat Mass Transfer*, vol. 39, pp. 579–587, 2003.
[90] T. J. Baker, Potential Flow Calculation by the Approximate Factorization Method, *J. Comput. Phys.*, vol. 42, pp. 1–19, 1981.

[91] H. A. Van Der Vorst, BiCGSTAB: A Fast and Smoothly Converging Variant of BICG for the Solution of Non-Symmetric Linear System, *SIAM (Soc. Ind. Appl. Math.) J. Sci. Stat. Comput.*, vol. 13, pp. 631–644, 1992.
[92] N. N. Smirnov, V. B. Betelin, R. M. Shagaliev, V. F. Nikitin, I. M. Belyakov, Yu. N. Deryuguin, S. V. Aksenov, and D. A. Korchazhkin, Hydrogen Fuel Rocket Engines Simulation using LOGOS Code, *Int. J. Hydrogen Energy*, vol. 39, pp. 10748–10756, 2014.
[93] V. B. Betelin, R. M. Shagaliev, S. V. Aksenov, I. M. Belyakov, Yu. N. Deryuguin, D. A. Korchazhkin, A. S. Kozelkov, V. F. Nikitin, A. V. Sarazov, and D. K. Zelenskiy, Mathematical Simulation of Hydrogen-Oxygen Combustion in Rocket Engines using LOGOS Code, *Acta Astronaut.*, vol. 96, pp. 53–64, 2014.
[94] Z. J. Zhu and H. X. Yang, Discrete Hilbert Transformation and Its Application to Estimate the Wind Speed in Hong Kong, *J. Wind Eng. Ind. Aerodynam.*, vol. 90, pp. 9–18, 2002.
[95] H. Tennekes and J. L. Lumley, *A First Course in Turbulence*, MIT Press, Cambridge, pp. 146–195, 1974.
[96] U. Frisch, *The Legacy of A. N. Kolmogorov, in Turbulence*, Cambridge University Press, pp. 81–88, 1995.
[97] M. Mihiev, Fundamentals of Heat Transfer, National-Thermodynamic Publisher, Moscow, Russia, pp. 1–392, 1956 (In Russian).

Appendix A. Numerical test of sub-grid viscosity

To compare the present SGM with that developed by Vreman [51], a three-dimensional flow field based on the analysis of thermal instability of a layer of fluid heated from below with the effect of rotation [68] is selected, the flow field is given by

$$\begin{cases} v_1 = -\frac{\pi}{a^2}\left[a_x \sin(a_x x)\cos(a_y y) + \frac{\sqrt{T}}{\pi^2+a^2} a_y \cos(a_x x)\sin(a_y y)\right] W_0 \cos(\pi z) \\ v_2 = -\frac{\pi}{a^2}\left[a_y \cos(a_x x)\sin(a_y y) - \frac{\sqrt{T}}{\pi^2+a^2} a_x \sin(a_x x)\cos(a_y y)\right] W_0 \cos(\pi z) \\ v_3 = W_0 \cos(a_x x)\cos(a_y y)\sin(\pi z) \end{cases} \tag{A.1}$$

In the numerical test, we assign $a_x = a_y = a/\sqrt{2}$, $a = \pi$, $W_0 = 1$, and the Taylor number $T = \frac{4\Omega^2}{\nu} d_0^4 = 1 \times 10^6$, where Ω is the angular speed of rotation around the z-axis, d_0 is the depth of the fluid layer, and ν is the fluid kinematic viscosity. The domain is given by $\{x \in (0, 2\sqrt{2}), y \in (0, 2\sqrt{2}), z \in (-1, 1)\}$ and is partitioned by $51 \times 51 \times 51$ grids. The grids are distributed uniformly in each direction. The calculated contours of the sub-grid viscosity are shown in Figures 1*a*, *b*. It can be seen that the sub-grid viscosity based on the present model is zero if the local flow is non-swirling, while sub-grid viscosity based on the Vreman's model does not hold.